# Kinematic Mapping of Giant Arcs: A New Method to Locate Lensing Critical Curves

Ruwen Zhou, 1,2,3 Liang Dai, Lingyuan Ji,4,2 Massimo Pascale,5 and Jose M. Diego<sup>6</sup>

<sup>1</sup> School of Physics and Technology, Wuhan University, Wuhan 430072, China
 <sup>2</sup> Department of Physics, 366 Physics North MC 7300, University of California, Berkeley, CA 94720, USA
 <sup>3</sup> Tsung-Dao Lee Institute, Shanghai Jiao-Tong University, Shanghai, 520 Shengrong Road, 201210, People's Republic of China
 <sup>4</sup> Berkeley Center for Cosmological Physics, University of California, Berkeley, CA 94720, USA
 <sup>5</sup> Department of Physics & Astronomy, University of California, Los Angeles, 430 Portola Plaza, Los Angeles, CA 90095, USA
 <sup>6</sup> Instituto de Física de Cantabria (CSIC-UC). Avda. Los Castros s/n. 39005 Santander, Spain

### ABSTRACT

Proximity of lensing critical curves features highly magnified portions of lensed galaxies. Accurate knowledge of the location and shape of the critical curve will be useful for understanding the nature of highly magnified stellar sources near critical curves and for revealing sub-galactic dark matter structures within the lens. In galaxy-cluster lenses, however, prediction of critical curves can be uncertain due to complexity in global mass modeling. Bracketing the critical curve with sparse lensed image pairs of compact continuum sources may not be sufficient as additional information available throughout the extended arc is not used. We explore and validate a kinematics-based method for locating the critical curve. This method leverages the continuous line-of-sight velocity profile of the lensed galaxy mapped through integral field spectroscopy of nebular emission lines, and combines an agnostic local lens model and a disk rotation model. Applying our method to a highly magnified region of the Dragon Arc in the Abell 370 cluster lensing field using archival Very Large Telescope (VLT)/Multi Unit Spectroscopic Explorer (MUSE) integral field unit (IFU) mapping of the H $\beta$  line, we constrain the critical curve to an uncertainty band with a half-width of 0.23'' ( $1\sigma$ ). This result reveals locations of recently detected extremely magnified stars biased toward the negative-parity side of the critical curve, as predicted for intracluster microlensing. With future James Webb Space Telescope (JWST)/Near-Infrared Spectrograph (NIRSpec) IFU mapping of the H $\alpha$  line at SNR  $\simeq 10$  (20), uncertainty could improve to 0.12" (0.08"). A measurement of this type with sufficiently small uncertainty may reveal small-scale wiggles in the shape of the critical curve where it crosses the giant arc, which can arise from the lensing perturbation of sub-galactic dark matter substructure. Our approach is generally applicable to caustic-crossing giant arcs in extragalactic lensing fields and can be incorporated into global lens modeling.

Keywords: Gravitational lensing (670), Galaxy clusters (584), Velocity maps (1767), Cosmology (343)

## 1. INTRODUCTION

One of the most spectacular situations of gravitational lensing involves a background galaxy overlapping a lensing caustic cast by a foreground galaxy or galaxy-cluster lens. Such a caustic-crossing galaxy often appears as a giant arc, which consists of multiple lensed images joining along lensing critical curves.

Corresponding author: Liang Dai liangdai@berkeley.edu

The vicinity of critical curve is highly interesting in strong lensing studies because it features a highly magnified portion of the giant arc. The lens map in this vicinity is often approximated by the fold model, which can be quantified using several parameters without having to involve full complexity in the global mass distribution of the lens (Schneider et al. 1992; Blandford & Narayan 1986). The most extremely magnified sources have small sizes and are uncovered near critical curves. For example,  $10^2-10^3$ -fold magnifications have enabled the detection of lensed individual luminous stars (Miralda-Escudé

1991) in  $z \sim 0.7-2$  galaxies with Hubble Space Telescope (HST) (Kelly et al. 2018; Rodney et al. 2018; Chen et al. 2019; Kaurov et al. 2019; Kelly et al. 2022) and JWST (Diego et al. 2023a; Yan et al. 2023; Fudamoto et al. 2024) imaging. Those are identified as photometric transients due to intracluster microlensing (Venumadhav et al. 2017; Diego et al. 2018; Oguri et al. 2018; Diego 2019; Weisenbach et al. 2024). They will allow us to characterize individual massive stars in the young Universe (Windhorst et al. 2018; Han & Dai 2024; Lundqvist et al. 2024; Zheng et al. 2025), study massive star populations and initial mass functions (Diego et al. 2024a; Li et al. 2025a,b; Palencia et al. 2025), and reveal invisible small-scale dark matter structures (e.g. Dai et al. 2018; Dai & Miralda-Escudé 2020; Williams et al. 2023; Müller & Miralda-Escudé 2025; Broadhurst et al. 2025). Additionally, candidate lensed individual stars with persistent fluxes have been discovered in higher-z caustic crossing galaxies (Welch et al. 2022; Diego et al. 2023b; Furtak et al. 2024; Choe et al. 2024), although some may be clusters of stars (see e.g. Pascale & Dai 2024; Ji & Dai 2025; Pascale et al. 2025a). Moreover, observations of highly magnified stellar clumps near caustics have offered insight into clustered star formation in extremely dense environments across a range of redshifts (e.g. Pascale et al. 2023; Vanzella et al. 2023; Adamo et al. 2024; Pascale et al. 2025a). Studying the positions and flux ratios of their lensed image pairs that straddle the critical curve sensitively probes sub-galactic dark matter (DM) sub-structures (Dai et al. 2020; Perera et al. 2025).

The exact location and shape of the lensing critical curve intersecting a giant arc carry valuable information in the study of high magnification lensing phenomena. For microlenses behaving as point masses such as stars or compact objects, theory predicts that micro critical curves fully interconnect within a band on the negative-parity side of the macro critical curve (Figure 4 of Venumadhav et al. 2017). As a result, microlensed individual stars are more detectable on the negativeparity side than on the positive-parity side. This is also reflected in the probability distribution function of the microlensing magnification factor depending on macro convergence and shear (e.g. Palencia et al. 2024). Such behavior of highly magnified stars is seen in the z=0.94caustic-crossing "Warhol" arc (Broadhurst et al. 2025). If instead an underlying population of diffuse small-scale DM structures dominate microlensing, such asymmmetry may be much weaker or absent.

This bias in the spatial distribution of microlensed stars has also been considered for distinguishing between sub-galactic clumpy structures resulting from either wavy dark matter or particle dark matter (Broadhurst et al. 2025). Moreover, critical curves are susceptible to perturbations from nearby small-scale DM clumps such as sub-galactic DM subhalos expected in the Cold Dark Matter (CDM) paradigm. It has been shown that across the width of the arc the critical curve may exhibit a wiggly shape owing to substructures (Dai et al. 2018; Williams et al. 2023; Ji & Dai 2025; Broadhurst et al. 2025).

While the critical curve intersecting the arc can be crudely located based on a mirror symmetry in the surface brightness profile on both sides, a precision determination is far from trivial. Blending of continuum surface brightness features and caustic transients in the lensed galaxy cause ambiguity in identifying lensed image pairs with the smallest separations straddling the critical curve. Magnification perturbations from subgalactic DM subhalos on small sources may further add confusion to this approach (Dai et al. 2020; Williams et al. 2023). Global lens models would ideally predict the exact location of critical curves. In practice, cluster-scale macro models suffer from mass modeling uncertainties, which are especially problematic when it comes to regions of high magnification.

The Dragon Arc is a spiral galaxy at z=0.725 lensed by the galaxy cluster Abell 370, and is one of the first lensed arcs known to astronomers. It has become a prime target for studying extreme magnification phenomena in cluster lensing fields after the recent detection of many highly magnified stars with HST (Kelly et al. 2022) and JWST (Fudamoto et al. 2024). However, independent macro lens models predict critical curve locations that differ at the (sub-)arcsecond level at some places on the arc (see Figure 1).

For another example, the locations of critical curve crossings are uncertain between multiple lens models in at least one immensely stretched portion of the z = 2.37Sunburst Arc (Pignataro et al. 2021; Diego et al. 2022; Sharon et al. 2022), where a highly-magnified young star cluster candidate Godzilla is situated (Vanzella et al. 2020; Diego et al. 2022; Pascale & Dai 2024; Choe et al. 2024). Similarly, the host galaxies of multiply-imaged Type Ia supernovae in PLCK G165.7+67.0 (Frye et al. 2024) and MACS J0138-2155 (Pierel et al. 2024) which have been used to measure the Hubble constant (Pascale et al. 2025b; Suyu et al. 2025) lack photometrically identified symmetries that can pinpoint the critical curve to sub-arcsecond precision. The placement of the critical curve affect both time delay and magnification predictions in lens models, which propagate directly to the  $H_0$  measurement. Important for cosmology, strong constraints on its location may provide avenue for refinement of these lensing systems. All these outstanding

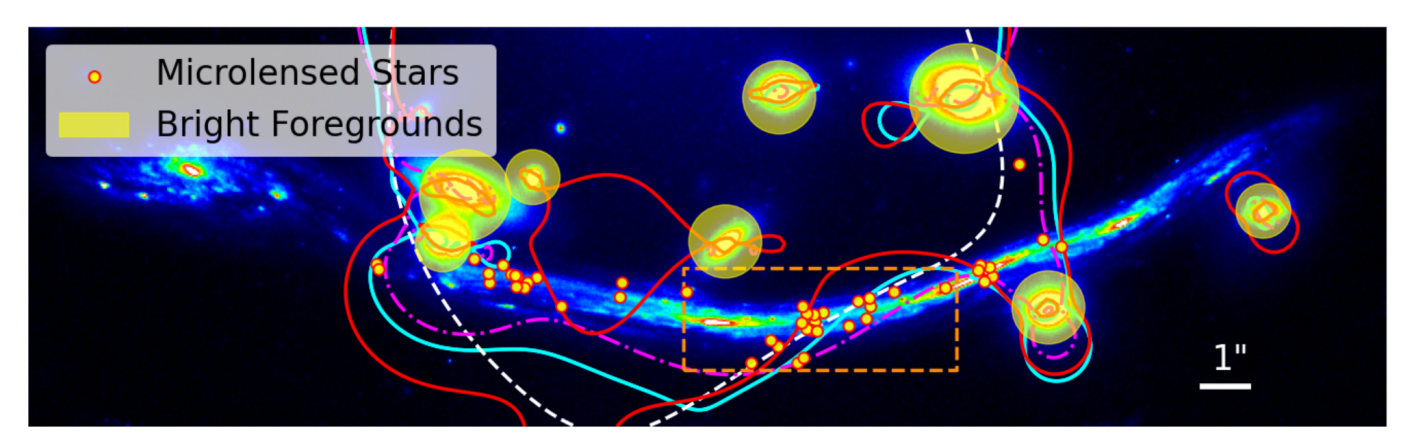


Figure 1. JWST NIRCam F090W image of Dragon Arc in the lensing field of galaxy cluster Abell 370. Bright foreground galaxies and stars are masked in yellow. Critical curves for the source redshift  $z_s = 0.725$  (Richard et al. 2010) are overlaid following the prediction of four lens models: Williams v4.1 (dashed white; Sebesta et al. 2016), Zitrin-Gauss v1.0 (dashed purple; Zitrin et al. 2009, 2013) based on the Light-Traces-Mass method, BUFFALO v1.0 (red solid; Niemiec et al. 2023) and the lastest hybrid WSLAP+ lens model (cyan solid; Diego et al. 2025a) constrained by JWST data. The orange rectangle highlights one highly magnified intersection between the critical curve and the giant arc, where two images of the lensed galaxy with opposite parity join together. While surface brightness patterns hint at roughly where critical curves cross the arc, the precise locations are uncertain. Yellow filled circles mark a few dozen microlensed red supergiant stars discovered by (Fudamoto et al. 2024), which are anticipated to primarily show in the vicinity of the critical curve (Dai et al. 2018).

challenges motivate the development of empirical methods to reliably locate critical curves to  $\sim 0.1''$  precision or better.

In this work, we exploit kinematic information to measure critical curve locations, and consider the Dragon Arc in Abell 370 as an excellent case study. Our empirical approach will complement extensive global lens modeling campaigns (Zitrin et al. 2013; Sebesta et al. 2016; Lagattuta et al. 2017; Niemiec et al. 2023; Diego et al. 2025b; Eid & Keeton 2025b), whose results typically depend on the choice of astrometric lensing constraints as well as lens mass parameterization. With medium resolution ( $R \simeq 3000$ ) integral field spectroscopy, the lineof-sight velocity across the lensed arc, which reflects rotation of the galaxy, can be measured from strong nebular emission lines such as  $H\alpha$ ,  $H\beta$ , [O II] $\lambda\lambda3726,3728$ and [O III] $\lambda\lambda 4959.5007$ . Compared to stellar photospheric emissions, nebular lines are spatially smoother, and are measurable throughout the entire region of interest. Since a static gravitational lens does not change the photon wavelength, the line-of-sight velocity profile exhibits a rough mirror symmetry on both sides of the critical curve along the direction of arc elongation. This general behavior reveals the true location of the critical curve independently of lens mapping far from it.

While kinematic mapping is a widely practiced technique to study gas dynamics in giant arcs (e.g. Girard et al. 2019; Di Teodoro et al. 2018; Patrício et al. 2018), a much smaller body of works have used kinematic information to constrain lens models (Young et al. 2022) and in particular the behaviors of critical curves. Focusing

on a promising target for the science of highly magnified stars, we apply this method to the Dragon Arc, analyze archival VLT/MUSE data, and assess the potential of using JWST/NIRSpec IFU observation.

The remainder of this paper is organized as follows. Section 2 summarizes archival data used in this study. In Section 3, we detail our methodology, starting with an introduction to the principles of velocity mapping of lensed galaxies, followed by descriptions of the disk rotation model and a polynomial local lens model. Section 4 validates the method via simulations: we construct a simulated Dragon Arc, based on the M74 galaxy, and generate mock observations under both JWST/NIRSpec and VLT/MUSE configurations. Bayesian inference is then applied to constrain the model parameters. Section 5 presents inference on the critical curve from applying the method to both simulated and archival VLT/MUSE data, as well as to simulated JWST/NIRSpec observations. In Section 6, we will discuss the limitations of the current approach, potential improvements, and future applications. Concluding remarks will be given in Section 7. In Appendix A, we study robustness of our results on the critical curve location against uncertainty in disk rotation modeling.

### 2. DATA

This work utilizes archival VLT/MUSE IFU spectroscopy datacube and JWST/NIRCam images of the Abell 370 field, along with VLT/MUSE IFU datacube of the grand design spiral galaxy M74 (NGC 0628).

JWST/NIRCam images of Abell 370 were obtained from the CANUCS program (GTO 1208; PI: Chris Willott). Data reduction and mosaic creation are performed by the MAGNIF collaboration using a modified reduction pipeline.

VLT/MUSE IFU spectroscopy data for Abell 370 are retrieved from the ESO archive under programs 094.A-0115(A) (PI: Johann Richard) and 096.A-0710(A) (PI: Franz E. Bauer). These observations were conducted under the WFM-NOAO-N mode, with spatial resolutions limited by seeing. The datacube covers the wavelength range 475–953 nm at a spectral resolution R  $\simeq 3000$  and is sampled at  $0.2^{\prime\prime}/\mathrm{pixel}$ .

The data were reduced with the standard ESO MUSE pipeline (v1.6.1).

We also use VLT/MUSE IFU spectroscopy data of M74 to create mocks. These were obtained from the ESO archive under programs 094.C-0623(A) (PI: Kathryn Kreckel), 095.C-0473(A) (PI: Guillermo A. Blanc) and 098.C-0484(A) (PI: Guillermo A. Blanc). These observations were conducted in the WFM-NOAON mode, cover 475—935 nm at R  $\simeq$  2830, and have an average seeing FWHM= 0.66" (about 30 pc at the distance of M74). The data were reduced with the standard ESO MUSE pipeline (v2.8.1).

### 3. METHOD

Our method requires several properties of the background lensed galaxy: (1) it must overlap with lensing caustics; (2) it must be a star-forming galaxy powering diffuse nebular lines; (3) the ideal source galaxy will have a rotating disk at a sizable inclination angle.

### 3.1. Kinematic Mapping with Nebular Lines

The disk of the Dragon Arc galaxy is inclined by 45-60 deg relative to the line of sight. After being mapped onto the image plane, the line-of-sight velocity profile exhibits a clear Doppler-shift pattern dominated by disk rotation. Shown in Figure 2, such a profile is clearly measured from the H $\beta$  line in the archival VLT/MUSE IFU data. The stronger  $H\alpha$  line falls outside the wavelength coverage. We adopt  $H\beta$  as the primary kinematic tracer instead of the strong metal forbidden doublet [O III] $\lambda\lambda 4959,5007$ . The H $\beta$  line has a relatively uniform spatial distribution, adequately tracing gas kinematics throughout the entire galaxy. In contrast, the spatial profile of [O III] doublet is more clumpy as a high ionization parameter in the vicinity of hot stars is required to excite doubly ionized oxygen. Looking forward to IFU spectroscopy with JWST/NIRSpec, the redshifted  $H\alpha$ line will be accessible using the G140H/F070LP grating/filter combination.

Lensing by a static gravitational potential does not change the photon wavelength. Given the typical line widths of H II regions  $\sigma_v > 1\text{--}10\,\mathrm{km/s}$ , the assumption of time independence is a good one. Thus, emission lines on the image plane on different sides of the critical curve but originated from the same region on the source plane show the same line-of-sight velocity.

In Figure 3, we examine the  $H\beta$  line within the highly magnified region defined by the orange rectangle in Figure 1 where the critical curve intersects the arc. When scanning through the  $H\beta$  line in wavelength space, bright regions associated with H II regions first appear on the east and west ends of the arc and progressively shift toward the critical curve from both directions. Bright emissions eventually disappear on the critical curve as the corresponding H II regions hide on the other side of the caustic. This variation in wavelength space reflects the Doppler effect across the disk, while disappearance of brightness on the critical curve is expected from the symmetry of lens map near a fold caustic.

## 3.2. Velocity Measurement

Mapping of line-of-sight velocity through IFU spectroscopy has been applied to studying gas kinematics in lensed giant arcs (Girard et al. 2019). For example, disk rotation of the magnified z=1.49 host spiral galaxy of SN Refsdal in the galaxy cluster MACSJ1149.5+2223 is measured based on the [O II] doublet and a flat rotation curve is recovered (Di Teodoro et al. 2018). Using a similar strategy, Patrício et al. (2018) modeled the disk rotation of 8 highly magnified galaxies at 0.6 < z < 1.5 including the Dragon Arc. However, these previous works did not specifically study lensing critical curves with kinematic mapping, which is the focus of this work.

Prior to measuring the line-of-sight velocity from the IFU datacube, we apply Wiener deconvolution, a classical non-blind deblurring method (see e.g. Wiener 1949; Orieux et al. 2010), to obtain an optimal estimate of the intrinsic spectral signal. This preprocessing is applied to each wavelength channel of the datacube. This is essential for mitigating the combined effects of finite telescope aperture and atmospheric turbulence, which cause blurring of the intrinsic line emission profile on the giant arc. Such degradation manifests as reduced spatial resolution and line signal mixing between neighboring source regions. Through mock measurements, we find that skipping preprocessing with Wiener deconvolution causes a bias in the velocity measurement, which leads to a bias in the inferred location of the critical curve.

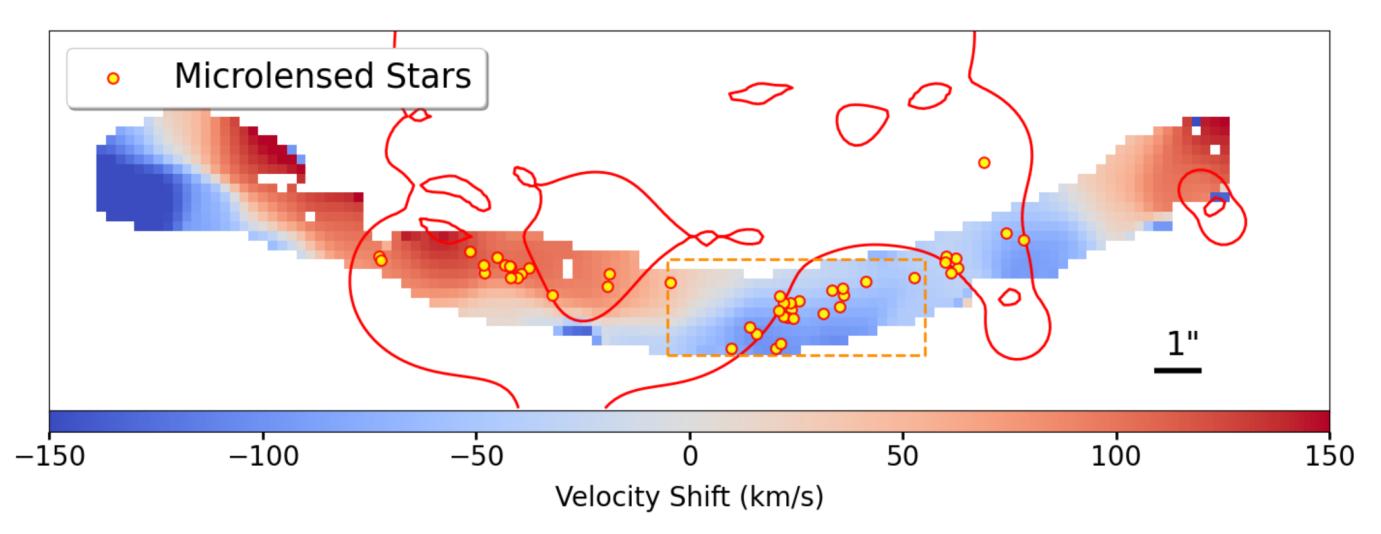


Figure 2. Line-of-sight velocity profile on the Dragon Arc derived from the H $\beta$  line using MUSE IFU data. Red and blue regions trace H II regions redshifted and blueshifted with respect to the reference velocity, respectively. Some pixels near the arc edge showing anomalous velocity values are likely contaminated by foreground galaxies. The red solid line shows the critical curve at  $z_s = 0.725$  from the BUFFALO lens model (Niemiec et al. 2023). One region of critical curve intersection, as enclosed by the orange rectangle in Figure 1, is where many microlensed individual highly magnified stars are detected through JWST imaging (Fudamoto et al. 2024).

For VLT/MUSE IFU observations under the NFM-NOAO mode, ground-based imaging is significantly compromised by poor seeing.

We approximate the PSF with a Moffat profile (Trujillo et al. 2001)

$$PSF(r) = \frac{\beta - 1}{\pi \alpha^2} \left[ 1 + \left(\frac{r}{\alpha}\right)^2 \right]^{-\beta}, \tag{1}$$

where  $\alpha$  is the scale radius of the core, and  $\beta$  governs the asymptotic decline of the wings as  $\mathrm{PSF}(r) \sim r^{-2\beta}$ . We empirically determine  $\alpha \simeq 0.5''$  and  $\beta \simeq 1.4$  by measuring unresolved foreground stars in the FoV.

Later when we make forecast for JWST/NIRSpec IFU observations, we will employ the Webbpsf tool (Perrin et al. 2014) to generate a model NIRSpec PSF kernel, thereby enabling reliable Wiener deconvolution.

With the Wiener-deconvolved datacube, we measure the  ${\rm H}\beta$  line center on the pixel-by-pixel basis, through the following steps:

- 1) Continuum subtraction:—We mask the  $H\beta$  line core and fit the neighboring continuum to a linear spectrum, which is then subtracted.
- 2) Peak identification:—We apply a peak-finding algorithm to the continuum-subtracted spectrum, selecting the most pronounced line feature near the systemic  $H\beta$  wavelength while rejecting noise-dominated peaks.
- 3) Gaussian fitting:—We fit the identified line to a Gaussian line profile with a free central wavelength and a free

Gaussian width, using flux uncertainty estimates provided in the archival MUSE datacube as weights in the fitting process.

4) Line-of-sight velocity:—The best-fit line central wavelength is converted to the line-of-sight velocity using the standard formula for Doppler redshift/blueshift.

Figure 4 shows an example in which we follow these procedures. The approach we outline above outputs a pixelized velocity map (such as the one in Figure 2) robust against spatial blurring and other noise effects.

Figure 2 shows the velocity map we derive using the H $\beta$  line in the archival MUSE IFU data. This dataset has a pixel scale of 0.2", an effective spatial resolution FWHM $\simeq$  0.7", and a spectral resolution of R  $\simeq$  3000. The median signal-to-noise ratio (SNR) per pixel in the H $\beta$  line is  $\simeq$  7.

Low spatial resolution eliminates information about velocity variation on small scales, preventing accurate localization of the critical curve below the smoothing scale and obscuring any possible small-scale curvilinear structure. The archival MUSE IFU dataset used here suffers significantly in this regard.

Spectral resolution is another crucial factor that is especially important when it comes to highly magnified regions adjacent to critical curves. Such regions map to a very small area on the source plane next to the caustic, across which only a small amount of differential rotation is present. That said, even at an instrumental spectral resolution that only modestly resolves the emission line profile, it is still possible to centroid the line center with

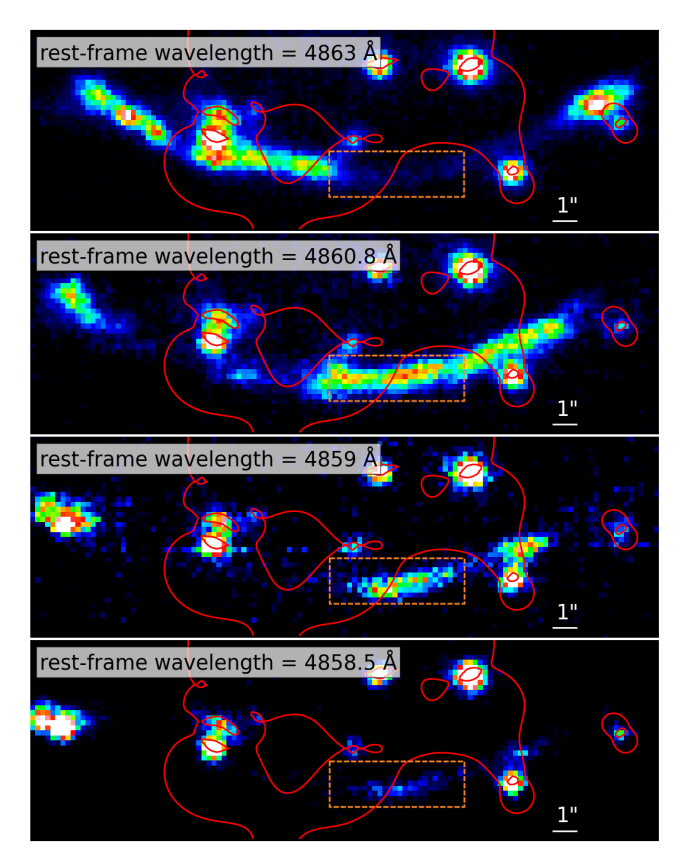


Figure 3. VLT/MUSE IFU data reveals variation of the line-of-sight velocity across the Dragon Arc. Surface brightness varies across the arc as one scans through the  ${\rm H}\beta$  line from 4863 Å to 4858.5 Å (rest frame). The red solid line shows the critical curve in the BUFFALO lens model (Niemiec et al. 2023). The behavior of the spatial surface brightness profile reveals roughly symmetric velocity patterns on both sides of critical curves, as expected from lens mapping near a fold caustic.

better precision if higher SNRs per spectral element are available, provided that the line profile model used is robust.

# 3.3. Velocity Profile on Image Plane

We require a parameterized model to fit the measured line-of-sight velocity field on the image plane, particularly in the vicinity of the critical curve. Through parameter inference, this will inform us about the behavior of the critical curve and provide uncertainty estimates. Our model consists of two independent major components: a disk rotation model, and a parameterized model of local lens map independent of global lens modeling.

### 3.3.1. Disk Rotation Model

Given that the Dragon Arc is a spiral galaxy, we consider a disk rotation model to define its primary kinematic structure. This simple model has 5 parameters:

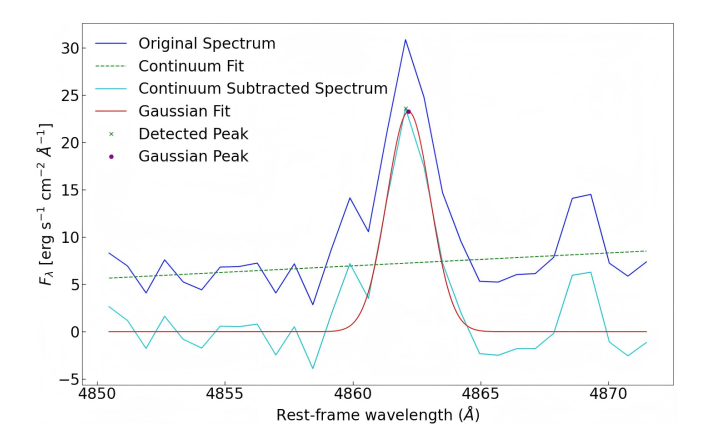


Figure 4. Example of Gaussian line profile fitting of the  $H\beta$  line with continuum subtraction applied to one particular pixel. The blue curve shows the original MUSE spectrum, and the dashed green line is a linear fit to the local continuum. The smooth red curve is the Gaussian fit to the continuum-subtracted spectrum (cyan), whose centroid (purple dot) is used to calculate the line-of-sight velocity.

 ${\rm RA_0}, {\rm DEC_0}, i, \phi, {\rm and}\ v_{\rm rot}.$  The position  $({\rm RA_0}, {\rm DEC_0})$  defines the kinematic center of the rotating disk on the source plane. The inclination angle i, ranging from  $0^\circ$  (face-on) to  $90^\circ$  (edge-on), affects the projection of the physical rotation velocity vector along the line of sight. The position angle  $\phi$  specifies the intrinsic orientation of the disk apparent major axis in the plane of the sky, measured from North  $(0^\circ)$  to East  $(+90^\circ)$ . Lastly,  $v_{\rm rot}$  is the circular velocity of disk rotation, which we approximate as independent of the galactocentric distance.

Projecting the circular disk rotation onto the line-ofsight direction, we find the line-of-sight velocity at any point on the source plane

$$v_{\text{los}} = v_{\text{rot}} \sin i \cos(\theta - \phi).$$
 (2)

Here  $\theta$  is the azimuthal position in the disk plane about the galaxy center, which can be easily found for the line of slight passing any point on the source plane and intersecting the disk. We have neglected a random velocity component for the H II regions.

In principle, the disk rotation curve can be calculated from a 3D mass model of the spiral galaxy and its host DM halo (Patrício et al. 2018). We assume a constant circular velocity  $v_{\rm rot}$  rather than a general radial function. A fairly "flat" rotation curve is found in typical spiral galaxies at 3–10 kpc (Sofue & Rubin 2001; de Blok et al. 2008; Lelli et al. 2016). It decently approximates some strongly lensed spiral galaxy (Di Teodoro et al. 2018). Moreover, the highly magnified region near the critical curve maps to a relatively small area on the source galaxy, which spans up to a few kpc around the turnover regime of the rotation curve. Over a limited

range of galactocentric distance, the rotation curve is approximately flat. This simple choice reduces the number of model parameters, but generalization to a more sophisticated parameterization of the rotation curve, if necessary, will be straightforward.

### 3.3.2. Local Lens Model

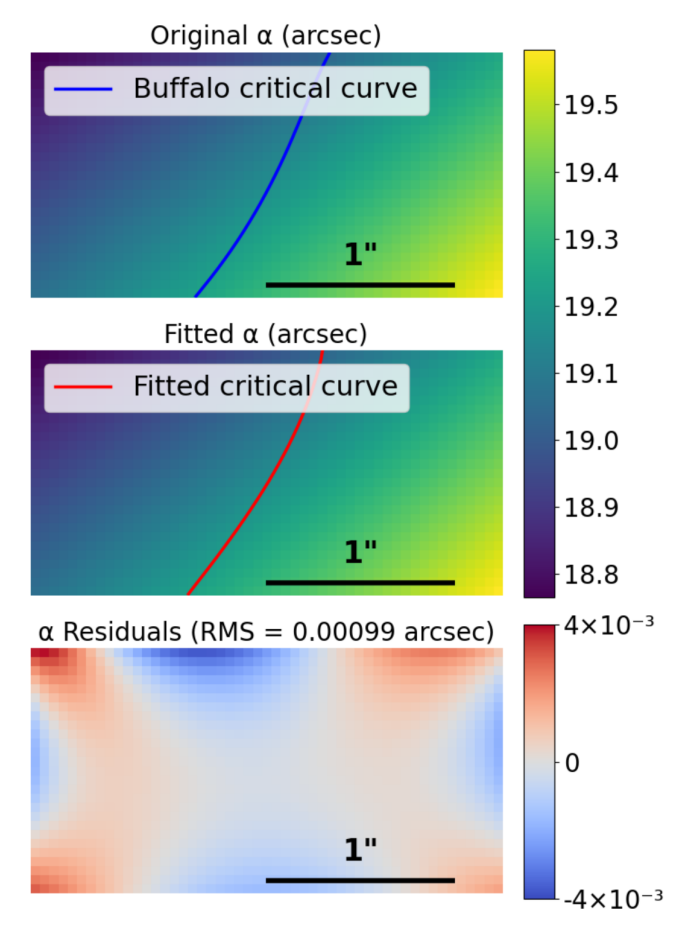


**Figure 5.** Fitting a 3rd-order polynomial deflection field to the BUFFALO lens model (Niemiec et al. 2023) in a  $2.5''\times1.3''$  vicinity of the critical curve. The magnitude of the deflection angle,  $\alpha=\sqrt{\alpha_1^2+\alpha_2^2}$ , is color-coded. The upper panel shows the original BUFFALO deflection field and the model critical curve (blue), while the middle panel shows the best-fit polynomial deflection field and the corresponding critical curve (red). The bottom panel shows that the fitting residuals have a root-mean-square (RMS) of  $\sim 0.001''$ .

To sufficiently describe lens mapping between the image plane and the source plane near the critical curves, we employ a third-order polynomial expansion for the deflection field. This approach goes beyond the simple fold caustic model (see e.g. Schneider et al. 1992; Blandford & Narayan 1986; Miralda-Escudé 1991), which has a limited range of validity near the critical curve. To exploit a sufficient amount of kinematic information, we

need to include a sizable portion of the arc extending on both sides of the critical curve. To this extent on the image plane, significant departure from the simple fold model is expected. A continuous deflection field in the form of a third-order polynomial is a parameterization flexible enough to capture general behavior of the local lens map regardless of the global mass model.

Define a Cartesian coordinate system  $(x_1, x_2)$  on the image plane (in angular units). We measure angular positions relative to a reference point  $(x_{0,1}, x_{0,2})$  through  $\Delta x_1 = x_1 - x_{0,1}$  and  $\Delta x_2 = x_2 - x_{0,2}$ . The deflection angle  $(\alpha_1, \alpha_2)$  is parameterized as

$$\alpha_{1} = a_{00} + a_{10} \Delta x_{1} + a_{01} \Delta x_{2}$$

$$+ a_{20} \Delta x_{1}^{2} + a_{11} \Delta x_{1} \Delta x_{2} + a_{02} \Delta x_{2}^{2}$$

$$+ a_{30} \Delta x_{1}^{3} + a_{21} \Delta x_{1}^{2} \Delta x_{2} + a_{12} \Delta x_{1} \Delta x_{2}^{2} + a_{03} \Delta x_{2}^{3},$$

$$(3)$$

$$\alpha_{2} = b_{00} + b_{10} \Delta x_{1} + b_{01} \Delta x_{2}$$

$$+ b_{20} \Delta x_{1}^{2} + b_{11} \Delta x_{1} \Delta x_{2} + b_{02} \Delta x_{2}^{2}$$

$$+ b_{30} \Delta x_{1}^{3} + b_{21} \Delta x_{1}^{2} \Delta x_{2} + b_{12} \Delta x_{1} \Delta x_{2}^{2} + b_{03} \Delta x_{2}^{3}.$$

For a Newtonian gravitational potential, and assuming a single lens plane, the deflection field is the gradient of the lensing potential (Schneider et al. 1992), so the polynomial coefficients are subject to constraints

$$b_{10} = a_{01},$$

$$b_{20} = a_{11}/2,$$

$$b_{11} = 2 a_{02},$$

$$b_{30} = a_{21}/3,$$

$$b_{21} = a_{12},$$

$$b_{12} = 3 a_{03}.$$
(5)

Since  $a_{00}$  and  $b_{00}$  are degenerate with RA<sub>0</sub> and DEC<sub>0</sub>, respectively, the original set of 20 polynomial coefficients reduces to 12 independent parameters:  $\{a_{10}, a_{01}, a_{20}, a_{11}, a_{02}, a_{30}, a_{21}, a_{12}, a_{03}\}$  for the Cartesian component  $\alpha_1$ , and  $\{b_{01}, b_{02}, b_{03}\}$  for the other Cartesian component  $\alpha_2$ .

The disk rotation model describes the intrinsic velocity field on the source plane, while the polynomial model for the deflection field determines mapping of the intrinsic velocity profile onto the image plane. These two ingredients are linked through the ray equation (Schneider et al. 1992),

$$y_i = x_i - \alpha_i(\vec{x}), \quad i = 1, 2.$$
 (6)

where  $(y_1, y_2)$  are angular coordinates on the source plane. Critical curves are found by requiring a degenerate Jacobian matrix  $A_{ij}$ 

$$\det A = \det \left( \delta_{ij} - \frac{\partial \alpha_i}{\partial x_j} \right) = 0. \tag{7}$$

We additionally convolve the model image-plane velocity profile with a two-dimensional Gaussian kernel whose width is a free parameter  $\sigma$ . While instrumental PSF smearing is treated with Wiener deconvolution, this does not perfectly undo it in the IFU data. We introduce in our model this *ad hoc* smearing effect to enhance effectualness of model fitting.

Figure 5 shows the effectualness of a 3rd-order polynomial model when it is employed to approximate the deflection field of the BUFFALO model (Niemiec et al. 2023) in a  $2.5'' \times 1.3''$  region centered on the critical curve.

In particular, we do not need to make the simplifying assumption that the critical curve is locally a straight line or an arc of a circle (Dai et al. 2018). A sizable curvature or more complex deformations can often be induced by nearby galaxy perturber lenses (Dai et al. 2020; Perera et al. 2025). Such departure from a simple straight critical curve is an important detail to consider for tangential arcs such as the Dragon Arc and the Sunburst Arc (Pignataro et al. 2021; Diego et al. 2022).

One more physical constraint we will implement is derived from the observed morphology of the arc. As can be seen in Figure 1, in the orange rectangular region arc elongation has an orientation in the range  $[0^{\circ}, 15^{\circ}]$  relative to the horizontal direction (West). This corresponds to the degenerate direction of the local lens mapping, which is set by the eigenvector of the Jacobian matrix  $A_{ij}$ . This is not enforced in the general polynomial model of ray deflection. We choose to constrain within this conservative range the degenerate direction evaluated at the center of the orange rectangular region, which is in the middle of the arc and very close to the recovered critical curve.

# 4. VALIDATION OF METHOD

To assess the fidelity of our method, we create mock IFU data that resembles the lensing situation of the Dragon Arc and perform kinematic mapping on the mock data. To that end, we require a nearby spiral galaxy whose nebular emission profile is measured at a spatial resolution well exceeding the level needed for analyzing strongly lensed galaxies at cosmological distances.

### 4.1. *M74*

For the purpose of creating mocks, we choose the local spiral galaxy M74, for which archival MUSE IFU data is available. This choice has several advantages:

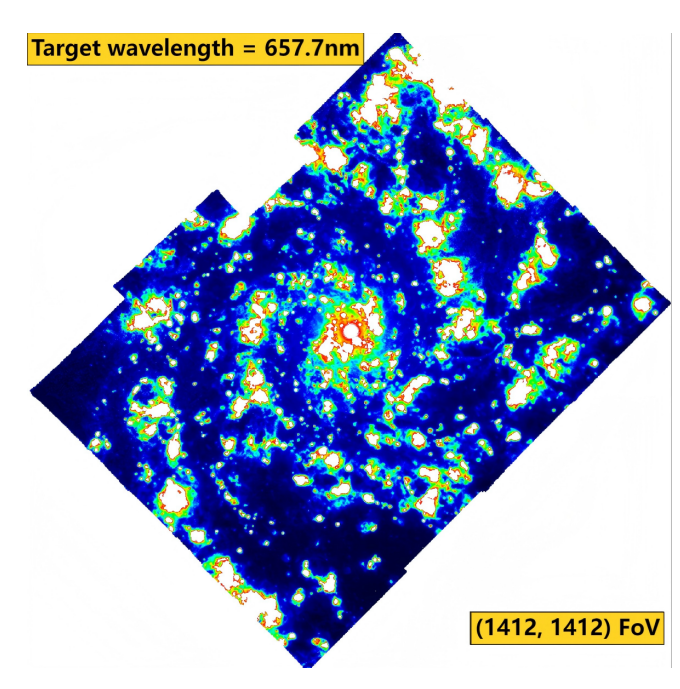


Figure 6. H $\alpha$  (observed at 657.7 nm) image of M74 (NGC 628) resolved down to  $\sim 30\,\mathrm{pc}$ , derived from archival MUSE IFU data. This galaxy is chosen as the source galaxy for creating mocks due to its grand-design spiral morphology, well-resolved H II regions, and nearly face-on orientation that simplifies kinematic analysis. Powered primarily by sites of star formation, the underlying spatial profile of H $\alpha$  surface brightness is clumpy. High-quality archival IFU data make it a favorable analog for the Dragon Arc, allowing for detailed forward modeling of lensing effects and instrumental effects.

- 1) Morphological similarity to Dragon Arc:—M74 is a "grand-design" spiral galaxy with well-defined spiral arms, making it an excellent analog for the Dragon Arc galaxy.
- 2) Well-resolved H II regions:—The distribution and properties of M74's discrete H II regions (Figure 6) help us better understand to what extent nebular emission can be approximated as spatially continuous when a similar galaxy at  $z \sim 1$  is imaged at a limited spatial resolution.
- 3) Face-On Orientation:—M74 is nearly face-on with a negligible Doppler effect due to disk rotation. Starting with a nearly zero inclination disk, we will artificially implement disk inclination in the synthetic data.

PHANGS-MUSE We use the public data M74(DR2 public release; IDNGC0628\_PHANGS\_DATACUBE\_native.fits) (Emsellem et al. 2022), acquired through 45 pointings over 23 observational blocks (2014-2017). The datacube covers the wavelength range 4759–9350 Å with  $\Delta \lambda = 1.25$  Å spectral sampling (R  $\simeq 2830$  at the wavelength of H $\alpha$ ),

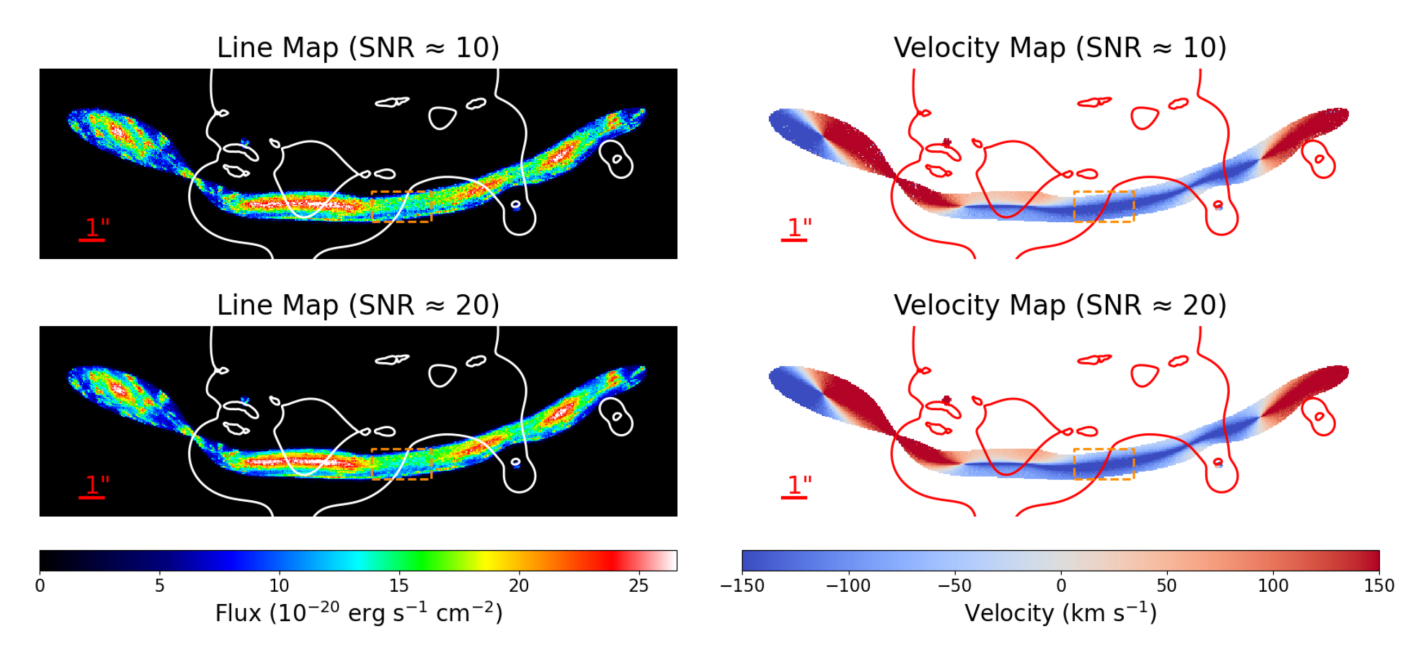


Figure 7. Mock IFU data of the Dragon Arc created for observational conditions appropriate for JWST/NIRSpec. See Section 3 for details. This mock data is used to validate the method of kinematic mapping in this work. Panels show flux map at the H $\alpha$  line (left) and the measured line-of-sight velocity (right), at two different noise levels (SNR  $\simeq$  10 and 20). The fold symmetry in the velocity value is visible on both sides of the critical curves. The critical curve (white in the left panels and red in the right panels) is derived from the interpolated BUFFALO model. The orange dashed rectangle (2.5"× 1.3") indicates the region of interest (ROI) of JWST configuration used for the Bayesian inference.

achieving a median SNR of 30 per spectral pixel in  ${\rm H\,{\sc ii}}$  regions.

## 4.2. Creating an Analog Galaxy

To create an analog of the lensed Dragon Arc galaxy based on observed nebular emissions in the local spiral M74, we go through the following procedures:

- 1) Emission Line Extraction:—We extract the H $\alpha$  line by isolating a narrow wavelength range around it pixel by pixel in the MUSE IFU datacube. Through the method described in Section 3.2, we perform pixel-by-pixel Gaussian line profile fitting to obtain a spatially well-resolved H $\alpha$  flux map with clearly identified H II regions.
- 2) Implementing Inclination:—While M74 is nearly face-on, we artificially implement a disk inclination of  $i=60^{\circ}$ . The corresponding Doppler shift in each pixel will be computed assuming a constant rotation curve of  $v_{\rm rot}=200\,{\rm km/s}$ .
- 3) Mock IFU Spectra:—For each spatial pixel, we fit a Gaussian  $H\alpha$  line to the original M74 spectrum and applying the required Doppler shift. The line width and flux are set accordingly to the original MUSE data, while the line center is shifted according to the disk rotation model and disk inclination. This procedure yields pixel-by-pixel synthetic spectra that consistently encode both disk rotation and intrinsic line properties.

The source-plane IFU data produced this way incorporate a realistic spatial distribution of H II regions and the prescribed kinematic properties.

# 4.3. Mock IFU Data

We need to create a mock giant arc that resembles the Dragon Arc observed with JWST/NIRSpec IFU. We create image-plane data by artificially lensing the mock spiral galaxy on the source plane with the BUFFALO macro lens model (Niemiec et al. 2023). We adjust the position and orientation of the mock spiral to roughly reproduce the morphology of the Dragon Arc. A NIR-Spec PSF model created with the Webbpsf package (Perrin et al. 2014) is then convolved with the image-plane data. To emulate realistic observational conditions, we renormalize the mean line flux to match what is observed in the MUSE data for Dragon Arc (converting  $H\beta$  flux to  $H\alpha$  flux assuming Case B recombination). We then include synthetic photon shot noise and readout noise to realize two different benchmark noise levels per pixel — SNR  $\simeq 10$  and SNR  $\simeq 20$  integrated over the H $\alpha$  line profile. For JWST/NIRSpec IFU, the finalized mock IFU datacube is mapped to a pixel scale of 0.05" (this pixel sampling, finer than the NIRSpec IFU instrumental sampling at 0.1" per pixel, is achievable through a dither pattern) and has a spectral resolution of  $R \simeq 3000$ .

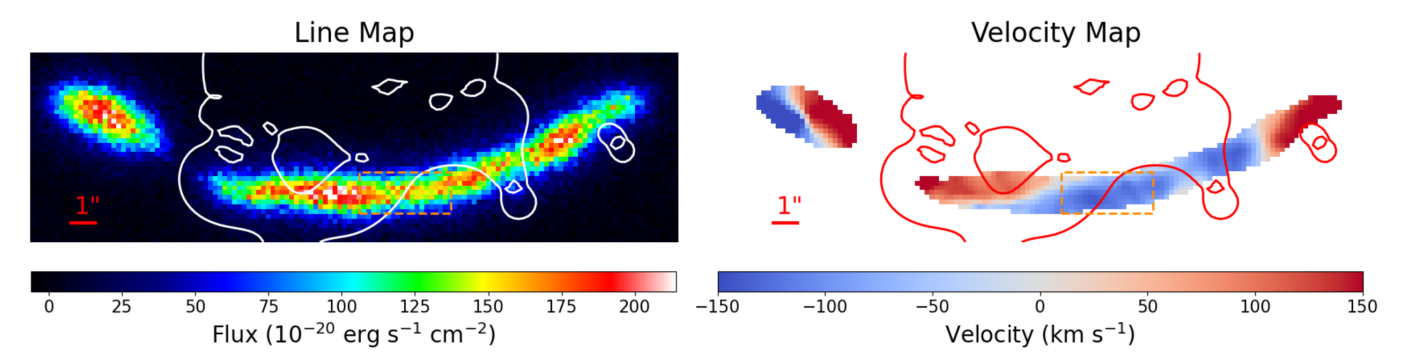


Figure 8. Simulated MUSE IFU data for a lensed spiral that resembles the Dragon Arc. Panels show the H $\beta$  flux per pixel (left) and the measured line-of-sight velocity field (right). The critical curve from the BUFFALO lens model is drawn. Bayesian modeling of disk rotation and lensing will be applied within the orange dashed rectangle (3.8"× 1.6").

Examples of this mock data are shown in Figure 7. The left two panels present the line maps at the two noise levels, while the right two panels display the corresponding velocity maps. These measurements are obtained following the methodology outlined in Section 3.2. We again emphasize the importance of performing Wiener deconvolution prior to measuring velocity. Using the PSF kernel generated by the Webbpsf tool (Perrin et al. 2014), deconvolution significantly reduces biases in the final Bayesian inference results. We will further make this point in the following sections.

Despite uncertainty in source galaxy properties and the macro lens model, which renders it difficult to perfectly replicate the Dragon Arc, our simulated arc reproduces many important features, such as topology and morphology of multiple images and fold symmetry. Both the line surface brightness and line-of-sight velocity profile resemble those of the Dragon Arc. This increases the credibility of our mock tests. As expected, the mock for JWST/NIRSpec IFU (Figure 7) has a superior quality than the archival VLT/MUSE data (Figure 2), with an improved pixel sampling (0.05" versus 0.2") and higher signal-to-noise ratios (SNR  $\simeq$  20 compared to SNR  $\simeq$  7 in MUSE).

For the mock VLT/MUSE IFU observation, we follow a procedure analogous to in the JWST/NIRSpec case but adapt to the corresponding instrumental characteristics. The MUSE mock (Figure 8) has a coarser pixel sampling of 0.2". The PSF is modeled as a Moffat profile (Section 3.2). Due to the MUSE wavelength coverage in this configuration, we use the H $\beta$  emission line instead of H $\alpha$ , scaling the line fluxes appropriately. We assume a moderately lower integrated SNR  $\simeq$  7 per pixel integrated over the H $\beta$  line. The mock datacube has a comparable spectral resolution ( $R \simeq 3000$ ) but Wiener deconvolution is less effective due to the coarser sampling and broader PSF.

## 4.4. Bayesian Inference

With mock arcs in hand under both the VLT/MUSE and JWST/NIRSpec IFU configurations, we validate our image-plane modeling of the velocity profile through Bayesian inference. The BUFFLO lens model is adopted as the ground truth for the lensing deflection field, which we aim to recover.

According to Bayes' theorem, the posterior probability distribution of the model parameters  $\Theta$  given the observed data  $\mathbf{d}$  is:

$$\mathcal{P}(\mathbf{\Theta}|\mathbf{d}) \propto \mathcal{L}(\mathbf{d}|\mathbf{\Theta}) \,\pi(\mathbf{\Theta})$$
 (8)

where  $\mathcal{L}(\mathbf{d}|\mathbf{\Theta})$  is the likelihood of observing  $\mathbf{d}$  given a model with parameters  $\mathbf{\Theta}$ , and  $\pi(\mathbf{\Theta})$  is the prior probability distribution for  $\mathbf{\Theta}$ . The likelihood function is defined as:

$$\mathcal{L}(\mathbf{d}|\mathbf{\Theta}) \propto \prod_{i \in \mathcal{M}} \exp \left\{ -\frac{1}{2} \left( \frac{v_{\text{obs},i} - v_{\text{pred},i}(\mathbf{\Theta})}{\sigma_{\text{obs},i}} \right)^2 \right\}$$
(9)

where  $\mathcal{M}$  denotes the set of valid pixelized data points within the diamond-shaped mask region. Here,  $v_{\text{obs},i}$  and  $v_{\text{pred},i}(\boldsymbol{\Theta})$  are the observed velocity and the model-predicted velocity, respectively, and  $\sigma_{\text{obs},i}$  is the corresponding uncertainty in velocity measurement.

We have the following set of model parameters:

$$\boldsymbol{\Theta} = \begin{cases} \text{RA}_0, \text{DEC}_0, i, \phi, v_{\text{rot}}; \\ a_{10}, a_{01}, a_{20}, a_{11}, a_{02}, a_{30}, a_{21}, a_{12}, a_{03}; \\ b_{01}, b_{02}, b_{03}; \\ \sigma \end{cases}$$

We employ uniform priors for all parameters with boundaries set sufficiently wide to encompass physically plausible values. However, we impose two important physical constraints on the lens model, as already discussed in Section 3.3.2. To ensure efficient and robust exploration of this high-dimensional parameter space, we adopt a two-stage inference strategy:

- 1) Global parameter optimization:—We first optimize  $\Theta$  using the differential evolution algorithm (implemented in SciPy). This step yields an initial estimate of the best-fit parameters.
- 2) Bayesian sampling:—We then use parameter values found by global optimization to initiate Markov Chain Monte Carlo (MCMC) runs using the emcee package (Foreman-Mackey et al. 2013).

We utilize the posterior samples of  $\Theta$  to derive the posterior distribution of the lensing critical curve. Recovery of the ground-truth critical curve from the BUFFALO model within the inference uncertainty will validate our methodology.

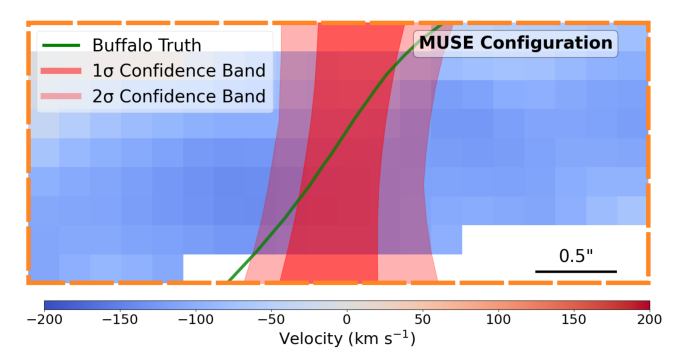


Figure 9. Mock measurements performed for the simulated lensed spiral galaxy as in Figure 11 and for the observational quality of VLT/MUSE IFU. The mean half width of the  $1\sigma$   $(2\sigma)$  confidence band is 0.25''(0.50''). While recovery is less accurate near the upper and lower edges due to insufficient pixels, the band is consistent with the true critical curve in the central part of the arc. Compared with the JWST NIR-Spec IFU case, the MUSE IFU results are more uncertain due to the significantly worse spatial resolution.

#### 5. RESULTS

We will discuss results separately under the two observational conditions considered: VLT/MUSE IFU and JWST/NIRSpec IFU.

## 5.1. VLT/MUSE IFU

Figure 9 presents a simulated measurement on the mock MUSE IFU data applied to the region of critical curve intersection bounded by the orange rectangle as in Figure 1.

Despite the poor spatial resolution, we are able to locate the critical curve to within a confidence band that has a half width of 0.25" at the  $1\sigma$  confidence level. The band has an orientation that differs moderately from that of the true critical curve, but is consistent within the posterior distribution.

We note that the quality of constraint from kinematic mapping alone sensitively depends on the specific realization of disk rotation on the source plane near the caustic. In Figure 9, the line-of-sight velocity varies by  $\lesssim 100\,\mathrm{km/s}$  throughout. At many places, the velocity profile along the direction of arc elongation is rather flat. If the line-of-sight velocity varied more strongly across that region, the local lens map and the critical curve would be better constrained.

In Figure 10, results are derived by applying our methodology to the real MUSE IFU data. We constrain the critical curve with a posterior half width of 0.23" at the  $1\sigma$  confidence level. If we relax the constraint on the local degenerate direction, the  $1\sigma$  half width inflates to 0.30". As expected, the critical curve is more tightly constrained in the middle of the arc than in the upper and lower outskirts.

Figure 10 shows residuals of  $\sim 10\,\mathrm{km/s}$  and correlated on  $\sim 0.5$ –1" scales. This may indicate a deficiency in the assumed disk rotation model, or distortions in the local lens map not captured by the polynomial model (which may be induced by sub-galactic DM subhalos), or unknown data analysis systematics. However, information is inadequate to draw robust conclusions.

Our derived confidence band has an orientation most similar to the prediction of the BUFFALO lens model (Niemiec et al. 2023), but shifts significantly to the West. This shifted location appears more consistent with the symmetric pattern of the continuum surface brightness, which is information we do not incorporate in modeling. Critical curves predicted by the two other models as shown in Figure 1 are at more shallow angles with respect to the arc and one of them is less compatible with the fold symmetry of the surface brightness profile. The confidence band is relatively more consistent with the non-parametric WSLAP+ lens model (Broadhurst et al. 2025; Diego et al. 2024b), which is strongly constrained by a dozen multiply-imaged surface brightness features identified across the Dragon Arc in deep HST and JWST images (Broadhurst et al. 2025).

Taking the middle of the confidence band to be our derived critical curve, about two-thirds of the microlensed highly magnified stars discovered in Fudamoto et al. (2024) fall on the side of negative parity. If the BUFFALO model critical curve is adopted, most microlensed stars would fall on the side of positive parity. The bias to negative parity is qualitatively consistent with microlensing by intracluster stars (Venumadhav et al. 2017), but we do not intend to compare to quantitative models as statistics are low here. Detection of many more microlensed stars in the Dragon Arc from upcoming JWST/NIRCam multi-epoch imaging (GO 7345; PI:

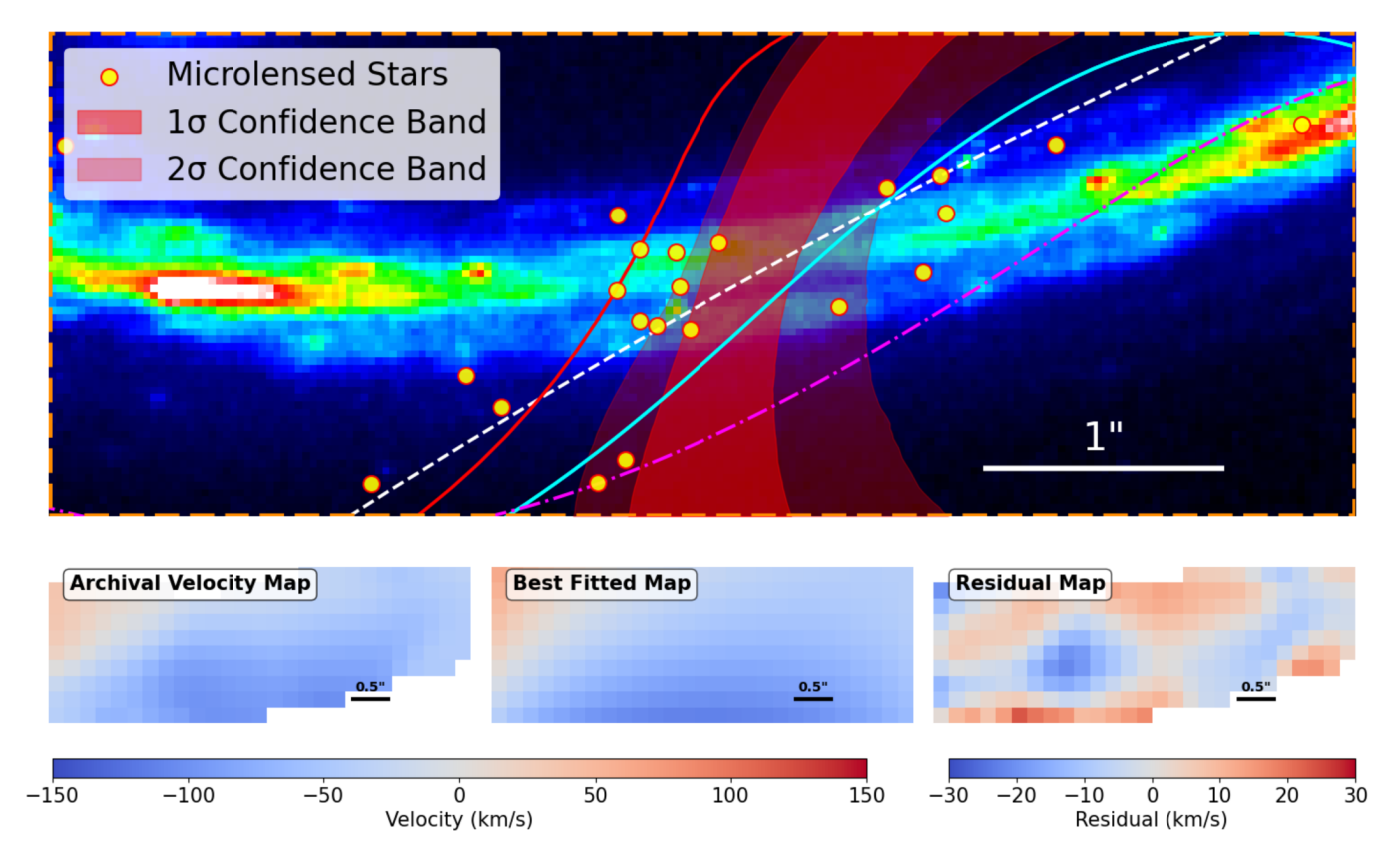


Figure 10. Upper panel: JWST NIRCam F090W image zoomed into the orange rectangular region marked in Figure 1, overlaid with the confidence bands for the critical curve derived using the H $\beta$  line from the archival MUSE data. The mean half width of the  $1\sigma$  ( $2\sigma$ ) confidence band is 0.23''(0.48''). Lower panel: (left) Image-plane line-of-sight velocity profile measured from the archival MUSE IFU data, (middle) the best-fit image-plane velocity profile, and (right) the corresponding residuals.

F. Sun) will mitigate Poisson fluctuations to allow quantitative studies.

From the posterior distribution of polynomial lens models, we compute the local gradient of the eigenvalue of the Jacobian matrix, defined as  $\mathbf{d} = -\nabla(\kappa + \lambda) = (|\mathbf{d}|\sin\alpha, -|\mathbf{d}|\cos\alpha)$  (Venumadhav et al. 2017). On the critical curve,  $\mathbf{d}$  has a magnitude  $|\mathbf{d}| = 7.7 \pm 1.3$  arcmin<sup>-1</sup> and  $|\mathbf{d}|\sin\alpha = 7.4 \pm 1.6$  arcmin<sup>-1</sup>, reflecting the angle  $\alpha$  between the critical curve and the degenerate direction.

**Table 1.** Derived disk parameters for the Dragon Arc: inclination i, position angle  $\phi$ , and rotation velocity  $v_{\rm rot}$ . We measure the position angle from North (0°) to East (+90°). We compare to Patrício et al. (2018), which is based on the global lens model of Lagattuta et al. (2017).

Parameter	Median	68% C.I.	Patrício et al. (2018)
$i \ [^{\circ}]$	70	(57, 78)	$54 \pm 1$
$\phi$ [°]	-38	(-43, -32)	$-30 \pm 3$
$v_{\rm rot} \ [{\rm km \ s^{-1}}]$	304	(267, 329)	$V_{\mathrm{max}} = 207 \pm 7$

Our derived  $v_{\rm rot} = 270-330 \,\mathrm{km/s}$  is larger than the typical range for spiral galaxies 200–250 km/s. While we find a disk orientation largely consistent with Patrício et al. (2018), our inferred  $v_{\rm rot}$  is significantly larger than the maximal velocity  $V_{\text{max}}$  there (Table 1). This discrepancy is attributed to several factors. First, we have adopted a simple flat rotation curve rather than one based on a physical galaxy mass model. More importantly, while in Patrício et al. (2018) disk parameters are recovered from the northeast lensed image of the full disk (see Figure 1), our local analysis in the orange rectangle fits only a part of it, which does not cover locations of extremal line-of-sight velocity values. In fact, we have set a broad prior  $150-350 \,\mathrm{km/s}$  for  $v_{\mathrm{rot}}$ to thoroughly explore the space of the local polynomial deflection field, but the posterior distribution piles up near the high end of the  $v_{\rm rot}$  prior, which reflects the limitation of kinematic fitting restricted to a part of the disk.

As we show in Appendix A, this limitation in recovering  $v_{\rm rot}$  does not compromise the ability to locate the critical curve. When we restrict  $v_{\rm rot}$  to a narrow prior  $195-205\,{\rm km/s}$ , a similar posterior distribution of critical

curves is derived, consistent with results derived without the tight prior on  $v_{\rm rot}$ . For the purpose of constraining the critical curve, the source-plane velocity field model does not have to be "physical". As long as the model can well fit the velocity field in the relevant source-plane region, fold symmetry guarantees additional robust information to constrain local lens mapping.

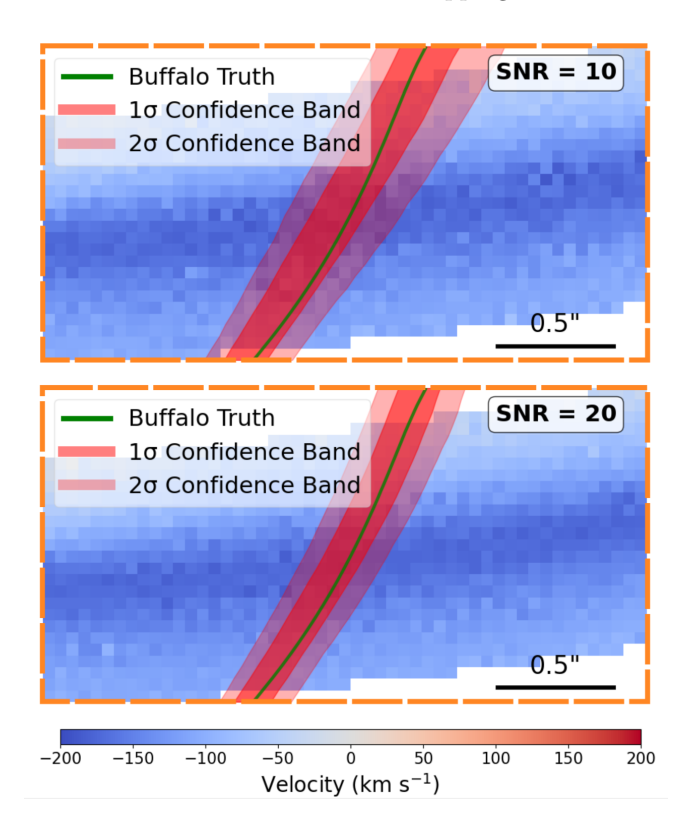


Figure 11. Constraints on the critical curve location from mock JWST NIRSpec IFU measurements, derived for the same simulated lensed spiral galaxy that resembles the Dragon Arc as in Figure 9, and at two different H $\alpha$  mean SNR levels (per pixel). Color-coded pixels show the line-of-sight velocity field (km/s) measured for the orange rectangular region shown in Figure 7, with red bands representing the  $1\sigma$  (dark red) and  $2\sigma$  (light red) confidence intervals. The green solid line shows the ground truth, which is the critical curve from the BUFFALO lens model. For SNR=10, the mean half width of the  $1\sigma$  ( $2\sigma$ ) confidence band is 0.12''(0.22''). For SNR=20, this improves to 0.08''(0.16''). In this example, the true position of the critical curve is recovered without bias.

## 5.2. Forecast for JWST/NIRSpec IFU

Figure 5 shows that a polynomial model fits the BUFFALO deflection field with negligible residuals < 0.005'' within the  $2.5'' \times 1.3''$  vicinity of the critical curve. A major difficulty, however, arises from the intrinsically shallow velocity profile across this region. The subtle

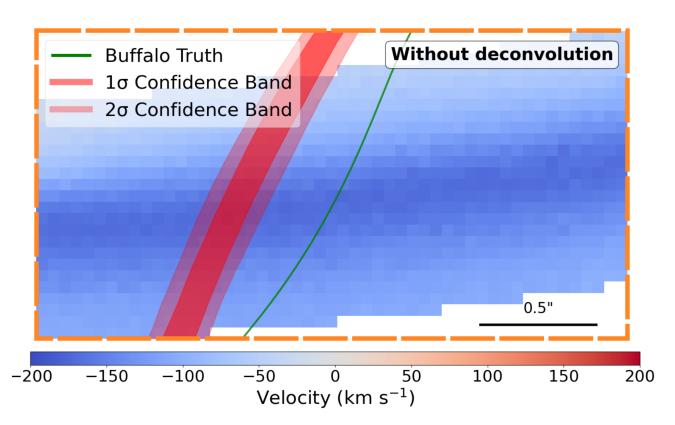


Figure 12. Mock JWST NIRSpec IFU measurement corresponding to the SNR  $\simeq 20$  case in Figure 11, but with velocities measured from IFU images without PSF deconvolution. In contrast to the results shown in Figure 11, Bayesian inference locates the critical curve with a large bias. In our method, PSF deconvolution proves essential in eliminating bias at VLT/MUSE and JWST NIRSpec IFU spatial resolutions.

velocity variation is easily washed out at the poor spatial resolution of MUSE, with the region having only  $12.5 \times 6.5$  pixels. To mitigate this, we have to fit the MUSE-derived velocity field in a larger field of view  $5.4'' \times 2.0''$  (Figure 10). Although the enlarged fitting region more effectively constrains the critical curve location, the effectualness of the polynomial deflection model degrades, resulting in relatively large velocity residuals.

We expect significant improvement if the same region is mapped with JWST/NIRSpec IFU, for which the PSF is smaller by a factor of  $\sim 6$ . For the same intrinsically shallow velocity profile, a smaller PSF and a finer pixel-sampling will allow the same gradient to be measured more accurately, and the polynomial deflection model may be used in a smaller vicinity of the critical curve.

Mock measurements performed under such conditions are presented in Figure 11, where the confidence band for the critical curve has a half width of only 0.12'' (0.08") at the  $1\sigma$  level if the  $H\alpha$  line is measured at SNR  $\simeq 10$  (20), a factor of  $\simeq 2{\text -}3$  improvement upon MUSE IFU. According to the JWST Exposure Time Calculator (ETC; Pontoppidan et al. 2016), about 8 hr (29 hr) of exposure is required to achieve SNR  $\simeq 10$  (20) per pixel.

The limitation will be dominated by the finite spectral resolution as well as systematics in modeling the sourceplane velocity profile and the local lens mapping.

At the superb imaging quality of JWST NIRSpec IFU, Wiener deconvolution or similar deconvolution algorithms will be a crucial step of preprocessing prior to reliable velocity measurements. Figure 12 shows that

without deconvolution our method yields a tight constraint on the critical curve location, which is however significantly biased from the ground truth.

### 6. DISCUSSION

In this section, we discuss limitations, potential improvements, and possible extensions of this work.

- 1) Additional Local Lens Constraints:—We have so far applied two constraints on the local lens map. The first one, Eq. 5, is the requirement of the lensing potential. The second one is an observational constraint on the elongation direction of the arc. In addition to these, image pairs of highly magnified stars identified in the future can be incorporated as additional constraints, although confidently identifying the image pair of the same lensed star may be non-trivial.
- 2) Improved Disk Rotation Model:—Our disk rotation model assumes a constant circular velocity  $v_{\rm rot}$ . While this is a simplification, it is well-motivated for the outer disk regions probed by the highly magnified arc, given the flat rotation curves observed in typical spiral galaxies at radii beyond a few kpc (Sofue & Rubin 2001; de Blok et al. 2008; Lelli et al. 2016). Nevertheless, one can readily incorporate more complex and realistic rotation curves, such as one derived for an exponential disk embedded in an Navarro-Frenk-White (NFW) (Navarro et al. 1996) dark matter halo. Additionally, the velocity model may allow a random velocity component for the H II regions reflecting ISM turbulence.
- 3) Improved Velocity Measurements:—We have used a simple linear model for local continuum fitting and assumes a Gaussian profile for emission lines. Both treatment can be improved for more physically realistic measurements. First, the stellar continuum could be modeled more rigorously using dedicated tools such as the PPXF code together with a library of stellar spectra, following the approach of Patrício et al. (2018). This may be particularly relevant in the case of the hydrogen Balmer lines for which a narrow nebular emission line is superimposed on top of a broad photospheric absorption line. Secondly, the assumption of a Gaussian line profile may be relaxed.
- 4) Generalization:—The applicability of our method is fundamentally rooted in its use of kinematic information, making it viable for any giant arc mapped with IFU spectroscopy. This allows us to utilize a variety of spectroscopic tracers across different wavebands: optical emission lines from H II regions for star-forming galaxies, photospheric absorption lines for quiescent galaxies, or molecular lines (e.g. with ALMA) for dusty, gas-rich

galaxies. The spectral information is not limited to the line center, but may also include parameters describing the line shape. Additionally, it will be powerful to incorporate kinematic information in global lens modeling and combine spectral information with other commonly used lensing constraints (Young et al. 2022).

5) Effects of Dark Matter Substructure:—The local lens map is expected to be perturbed by DM subhalos, which produces "wiggles" in the critical curve (Dai et al. 2018; Williams et al. 2023; Ji & Dai 2025; Perera et al. 2025). While a simple polynomial deflection field with enforced smoothness may not capture such perturbation, significant misfit with high-quality JWST/NIRSpec IFU data in the future may be a hint for the subhalos. To detect the effect of subhalos, the local lens mapping may be extended to allow sinusoidal spatial variations, which can be fit to data.

### 7. CONCLUSION

We have developed a method to determine the local lens map in the proximity of a lensing critical curve intersecting a giant arc, which relies on mapping the line-of-sight velocity across the arc using emission line data from IFU spectroscopy. Applied to spiral galaxies, it combines a local polynomial deflection field with a model disk rotation curve on the source plane. Assuming that the local deflection smoothly varies, the method locates the critical curve with uncertainty estimates. Through mock tests, we find that applying Wiener deconvolution to IFU images before velocity measurement eliminates the bias caused by instrumental PSF effects.

To specifically study the Dragon Arc in the lensing field of Abell 370, we have validated the method by creating a mock lensed galaxy having clumpy nebular emissions as in a real spiral, lensing it into an image-plane configuration similar to the Dragon Arc, and performing mock Bayesian inference.

Applying the method to archival VLT/MUSE IFU data for the Dragon Arc, we locate the critical curve, in one highly magnified region on the arc, with a  $1\sigma$  uncertainty of  $\sim 0.2''$ . The confidence band of our derived critical curve is narrow enough to differentiate from the prediction of some global lens models that leverage the deepest HST and JWST/NIRCam images. The results tentatively support the theory of microlensing by intracluster stars that the majority of detected microlensing events of highly magnified stars appear on the negative-parity side of the macro critical curve, while larger statistics of lensed stars are needed for confirmation

With diffraction-limited PSFs, JWST/NIRSpec IFU is expected to improve the constraint by  $\sim 2-3$  fold.

At high astrometric precision, a generalization of our approach that allows more degrees of freedom in the local lens map may uncover wiggly structures in the critical curve revealing small-scale dark matter substructures (Dai et al. 2018; Broadhurst et al. 2025; Perera et al. 2025). We expect that the fidelity of the method will hinge on model flexibilities that can capture features in disk rotation and lensing perturbations from sub-galactic dark matter structures, for which future studies are needed. Finally, kinematic information can be included in a global lens modeling procedure that ac-

counts for all available spatially resolved information on the extended giant arc (Eid & Keeton 2025b,a).

#### ACKNOWLEDGMENTS

R.Z. is grateful for the Berkeley Physics International Education (BPIE) program during which this research project was initiated. The authors would also like to thank Jessica Lu for useful discussions. L.D. acknowledges research grant support from the Alfred P. Sloan Foundation (Award Number FG-2021-16495), from the Frank and Karen Dabby STEM Fund in the Society of Hellman Fellows.

#### **APPENDIX**

## A. ROTATION VELOCITY PRIOR AND CRITICAL CURVE CONSTRAINTS

To verify that our derived constraint on the critical curve is not compromised by the limited capability to determine the global disk rotation velocity  $v_{\rm rot}$ , we perform an analysis assuming a narrow prior  $v_{\rm rot} = 195-205\,{\rm km/s}$ . This test confirms that an accurate inference on  $v_{\rm rot}$  is not necessary for correctly locating the critical curve.

As shown in Figure 13, the constraint on the critical curve is shown. The confidence band derived with the narrow  $v_{\rm rot}$  prior is very similar to that derived with the broad prior  $v_{\rm rot} = 150-350\,{\rm km\,s^{-1}}$  as shown in Figure 10. The middle part of the band is unchanged, with only modest offsets in the upper and lower outskirts of the arc where kinematic information is inadequate.

The mean half width of the  $1\sigma$  ( $2\sigma$ ) confidence band is 0.23'' (0.52''), virtually the same as the 0.23'' (0.48'') width derived using the broad prior. We also note that the velocity residual maps look nearly identical between the two cases.

Parameter inference from both analyses are compared in Table 2. While the disk orientation parameters  $(i, \phi)$  show slight differences, the quality of the best-fit, as indicated by the reduced  $\chi^2$  value, appears nearly identical. Most importantly, the constraint on the critical curve is consistent between the two cases. This suggests that our ability to constrain the critical curve is robust, even though, perhaps unsurprisingly, fitting a small part of the disk near the lensing caustic is inadequate for correctly reconstructing the global kinematic profile of the galaxy.

**Table 2.** Comparison of derived disk parameters and critical curve constraints using broad versus narrow priors for the rotation velocity  $v_{\text{rot}}$ . The position angle  $\phi$  is measured from North (0°) to East (+90°).

	Broad Prior (150–350 km/s)	Narrow Prior   (195–205 km/s)
Parameters (68% C.I.)		
$i \ [^{\circ}]$	(57, 78)	(69, 80)
$\phi \ [^\circ]$	(-43, -32)	(-46, -37)
$v_{\rm rot} \ [{\rm km \ s}^{-1}]$	(267, 329)	(198, 204)
Model Performance		
$\chi^2/\mathrm{dof}$ (best fit)	0.93	0.95
$1\sigma$ band [arcsec]	0.23	0.23
$2\sigma$ band [arcsec]	0.48	0.52

# REFERENCES

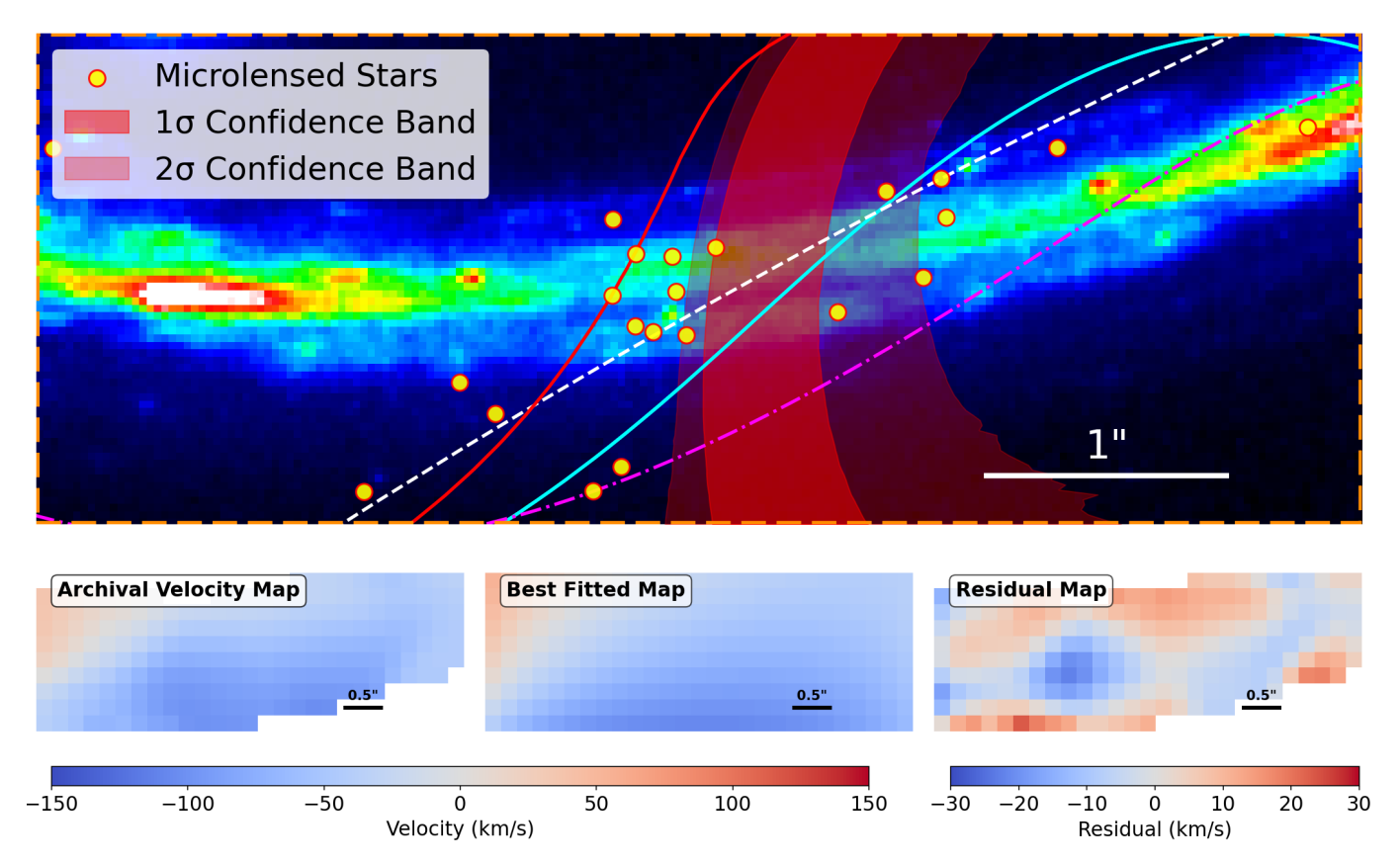


Figure 13. Critical curve constraints derived using a narrow prior on the rotation velocity ( $v_{\text{rot}} = 195-205 \,\text{km s}^{-1}$ ). The resulting confidence band is nearly identical to that obtained with a broad prior (see Figure 10), demonstrating the robustness of the critical curve localization. The mean half-width of the  $1\sigma$  ( $2\sigma$ ) confidence band is 0.23'' (0.52'').

Broadhurst, T., Li, S. K., Alfred, A., et al. 2025, ApJL, 978, L5, doi: 10.3847/2041-8213/ad9aa8

Chen, W., Kelly, P. L., Diego, J. M., et al. 2019, ApJ, 881, 8, doi: 10.3847/1538-4357/ab297d

Choe, S., Rivera-Thorsen, T. E., Dahle, H., et al. 2024, arXiv e-prints, arXiv:2405.06953, doi: 10.48550/arXiv.2405.06953

Dai, L., & Miralda-Escudé, J. 2020, AJ, 159, 49, doi: 10.3847/1538-3881/ab5e83

Dai, L., Venumadhav, T., Kaurov, A. A., & Miralda-Escud, J. 2018, ApJ, 867, 24, doi: 10.3847/1538-4357/aae478

Dai, L., Kaurov, A. A., Sharon, K., et al. 2020, MNRAS, 495, 3192, doi: 10.1093/mnras/staa1355

de Blok, W. J. G., Walter, F., Brinks, E., et al. 2008, AJ, 136, 2648, doi: 10.1088/0004-6256/136/6/2648

Di Teodoro, E. M., Grillo, C., Fraternali, F., et al. 2018, MNRAS, 476, 804, doi: 10.1093/mnras/sty175

Diego, J. M. 2019, A&A, 625, A84, doi: 10.1051/0004-6361/201833670

Diego, J. M., Pascale, M., Kavanagh, B. J., et al. 2022, A&A, 665, A134, doi: 10.1051/0004-6361/202243605

Diego, J. M., Kaiser, N., Broadhurst, T., et al. 2018, ApJ, 857, 25, doi: 10.3847/1538-4357/aab617 Diego, J. M., Meena, A. K., Adams, N. J., et al. 2023a, A&A, 672, A3, doi: 10.1051/0004-6361/202245238

Diego, J. M., Sun, B., Yan, H., et al. 2023b, A&A, 679, A31, doi: 10.1051/0004-6361/202347556

Diego, J. M., Li, S. K., Meena, A. K., et al. 2024a, A&A, 681, A124, doi: 10.1051/0004-6361/202346761

Diego, J. M., Li, S. K., Amruth, A., et al. 2024b, A&A, 689, A167, doi: 10.1051/0004-6361/202450474

Diego, J. M., Sun, F., Palencia, J. M., et al. 2025a, arXiv e-prints, arXiv:2506.11207,

doi: 10.48550/arXiv.2506.11207

—. 2025b, arXiv e-prints, arXiv:2506.11207, doi: 10.48550/arXiv.2506.11207

Eid, L., & Keeton, C. 2025a, arXiv e-prints, arXiv:2511.11952, doi: 10.48550/arXiv.2511.11952

Eid, L., & Keeton, C. R. 2025b, ApJ, 990, 196, doi: 10.3847/1538-4357/adf4cb

Emsellem, E., Schinnerer, E., Santoro, F., et al. 2022, A&A, 659, A191, doi: 10.1051/0004-6361/202141727

Foreman-Mackey, D., Hogg, D. W., Lang, D., & Goodman, J. 2013, Publications of the Astronomical Society of the Pacific, 125, 306–312, doi: 10.1086/670067

- Frye, B. L., Pascale, M., Pierel, J., et al. 2024, ApJ, 961, 171, doi: 10.3847/1538-4357/ad1034
- Fudamoto, Y., Sun, F., Diego, J. M., et al. 2024, arXiv e-prints, arXiv:2404.08045, doi: 10.48550/arXiv.2404.08045
- Furtak, L. J., Meena, A. K., Zackrisson, E., et al. 2024, MNRAS, 527, L7, doi: 10.1093/mnrasl/slad135
- Girard, M., Dessauges-Zavadsky, M., Combes, F., et al. 2019, A&A, 631, A91, doi: 10.1051/0004-6361/201935896
- Han, X., & Dai, L. 2024, ApJ, 964, 160, doi: 10.3847/1538-4357/ad2b6a
- Ji, L., & Dai, L. 2025, ApJ, 980, 190, doi: 10.3847/1538-4357/ada76a
- Kaurov, A. A., Dai, L., Venumadhav, T., Miralda-Escudé, J., & Frye, B. 2019, ApJ, 880, 58, doi: 10.3847/1538-4357/ab2888
- Kelly, P. L., Diego, J. M., Rodney, S., et al. 2018, Nature Astronomy, 2, 334, doi: 10.1038/s41550-018-0430-3
- Kelly, P. L., Chen, W., Alfred, A., et al. 2022, arXiv e-prints, arXiv:2211.02670, doi: 10.48550/arXiv.2211.02670
- Lagattuta, D. J., Richard, J., Clément, B., et al. 2017, MNRAS, 469, 3946, doi: 10.1093/mnras/stx1079
- Lelli, F., McGaugh, S. S., & Schombert, J. M. 2016, AJ, 152, 157, doi: 10.3847/0004-6256/152/6/157
- Li, S. K., Diego, J. M., Meena, A. K., et al. 2025a, ApJ, 988, 178, doi: 10.3847/1538-4357/ade4bd
- Li, S. K., Palencia, J. M., Diego, J. M., et al. 2025b, arXiv e-prints, arXiv:2506.17565, doi: 10.48550/arXiv.2506.17565
- Lundqvist, E., Zackrisson, E., Hawcroft, C., Amarsi, A. M., & Welch, B. 2024, A&A, 690, A291, doi: 10.1051/0004-6361/202450403
- Miralda-Escudé, J. 1991, ApJ, 379, 94, doi: 10.1086/170486
  Müller, C. V., & Miralda-Escudé, J. 2025, MNRAS, 536, 1579, doi: 10.1093/mnras/stae2652
- Navarro, J. F., Frenk, C. S., & White, S. D. M. 1996, ApJ, 462, 563, doi: 10.1086/177173
- Niemiec, A., Jauzac, M., Eckert, D., et al. 2023, MNRAS, 524, 2883, doi: 10.1093/mnras/stad1999
- Oguri, M., Diego, J. M., Kaiser, N., Kelly, P. L., & Broadhurst, T. 2018, PhRvD, 97, 023518, doi: 10.1103/PhysRevD.97.023518
- Orieux, F., Giovannelli, J.-F., & Rodet, T. 2010, Journal of the Optical Society of America. A Optics, Image Science, and Vision, 1593, doi: 10.1364/JOSAA.27.001593
- Palencia, J. M., Diego, J. M., Kavanagh, B. J., & Martínez-Arrizabalaga, J. 2024, A&A, 687, A81, doi: 10.1051/0004-6361/202347492

- Palencia, J. M., Diego, J. M., Dai, L., et al. 2025, A&A, 699, A295, doi: 10.1051/0004-6361/202555447
- Pascale, M., & Dai, L. 2024, ApJ, 976, 166, doi: 10.3847/1538-4357/ad7732
- Pascale, M., Dai, L., Frye, B. L., & Beverage, A. G. 2025a, ApJL, 988, L76, doi: 10.3847/2041-8213/aded93
- Pascale, M., Dai, L., McKee, C. F., & Tsang, B. T. H. 2023, ApJ, 957, 77, doi: 10.3847/1538-4357/acf75c
- Pascale, M., Frye, B. L., Pierel, J. D. R., et al. 2025b, ApJ, 979, 13, doi: 10.3847/1538-4357/ad9928
- Patrício, V., Richard, J., Carton, D., et al. 2018, MNRAS, 477, 18, doi: 10.1093/mnras/stv555
- Perera, D., Gilman, D., Williams, L. L. R., et al. 2025, arXiv e-prints, arXiv:2511.04748. https://arxiv.org/abs/2511.04748
- Perrin, M. D., Sivaramakrishnan, A., Lajoie, C.-P., et al. 2014, in Society of Photo-Optical Instrumentation
  Engineers (SPIE) Conference Series, Vol. 9143, Space
  Telescopes and Instrumentation 2014: Optical, Infrared, and Millimeter Wave, ed. J. M. Oschmann, Jr.,
  M. Clampin, G. G. Fazio, & H. A. MacEwen, 91433X, doi: 10.1117/12.2056689
- Pierel, J. D. R., Newman, A. B., Dhawan, S., et al. 2024, ApJL, 967, L37, doi: 10.3847/2041-8213/ad4648
- Pignataro, G. V., Bergamini, P., Meneghetti, M., et al. 2021, arXiv e-prints, arXiv:2106.10286. https://arxiv.org/abs/2106.10286
- Pontoppidan, K. M., Pickering, T. E., Laidler, V. G., et al. 2016, Observatory Operations: Strategies, Processes, and Systems VI, 9910, 991016, doi: 10.1117/12.2231768
- Richard, J., Kneib, J. P., Limousin, M., Edge, A., & Jullo, E. 2010, MNRAS, 402, L44, doi: 10.1111/j.1745-3933.2009.00796.x
- Rodney, S. A., Balestra, I., Bradac, M., et al. 2018, Nature Astronomy, 2, 324, doi: 10.1038/s41550-018-0405-4
- Schneider, P., Ehlers, J., & Falco, E. E. 1992, Gravitational Lenses, doi: 10.1007/978-3-662-03758-4
- Sebesta, K., Williams, L. L. R., Mohammed, I., Saha, P., & Liesenborgs, J. 2016, MNRAS, 461, 2126, doi: 10.1093/mnras/stw1433
- Sharon, K., Mahler, G., Rivera-Thorsen, T. E., et al. 2022, arXiv e-prints, arXiv:2209.03417. https://arxiv.org/abs/2209.03417
- Sofue, Y., & Rubin, V. 2001, ARA&A, 39, 137, doi: 10.1146/annurev.astro.39.1.137
- Suyu, S. H., Acebron, A., Grillo, C., et al. 2025, arXiv e-prints, arXiv:2509.12319, doi: 10.48550/arXiv.2509.12319

- Trujillo, I., Aguerri, J. A. L., Cepa, J., & Gutiérrez, C. M. 2001, MNRAS, 328, 977,
  - ${\bf doi:}\ 10.1046/j.1365\text{--}8711.2001.04937.x}$
- Vanzella, E., Meneghetti, M., Pastorello, A., et al. 2020,
  MNRAS, 499, L67, doi: 10.1093/mnrasl/slaa163
- Vanzella, E., Claeyssens, A., Welch, B., et al. 2023, ApJ, 945, 53, doi: 10.3847/1538-4357/acb59a
- Venumadhav, T., Dai, L., & Miralda-Escudé, J. 2017, ApJ, 850, 49, doi: 10.3847/1538-4357/aa9575
- Weisenbach, L., Anguita, T., Miralda-Escudé, J., et al. 2024, arXiv e-prints, arXiv:2404.08094, doi: 10.48550/arXiv.2404.08094
- Welch, B., Coe, D., Diego, J. M., et al. 2022, Nature, 603, 815, doi: 10.1038/s41586-022-04449-y

- Wiener, N. 1949, Extrapolation, Interpolation, and Smoothing of Stationary Time Series: With Engineering Applications (The MIT Press), doi: 10.7551/mitpress/2946.001.0001
- Williams, L. L. R., Kelly, P. L., Treu, T., et al. 2023, arXiv e-prints, arXiv:2304.06064, doi: 10.48550/arXiv.2304.06064
- Windhorst, R. A., Timmes, F. X., Wyithe, J. S. B., et al. 2018, ApJS, 234, 41, doi: 10.3847/1538-4365/aaa760
- Yan, H., Ma, Z., Sun, B., et al. 2023, ApJS, 269, 43, doi: 10.3847/1538-4365/ad0298
- Young, A. J., Keeton, C. R., & Baker, A. J. 2022, ApJ, 929, 6, doi: 10.3847/1538-4357/ac59af
- Zheng, W., Fu, X., Chen, Y., et al. 2025, ApJ, 987, 94, doi: 10.3847/1538-4357/add72a
- Zitrin, A., Broadhurst, T., Umetsu, K., et al. 2009, MNRAS, 396, 1985,
  - doi: 10.1111/j.1365-2966.2009.14899.x
- Zitrin, A., Meneghetti, M., Umetsu, K., et al. 2013, ApJL, 762, L30, doi: 10.1088/2041-8205/762/2/L30